Mon. Not. R. Astron. Soc. **380,** 489–498 (2007) doi:10.1111/j.1365-2966.2007.12104.x

Non-circular motion evidence in the circumnuclear region of M100 (NGC 4321)

A. Castillo-Morales,[1⋆] J. Jiménez-Vicente,[2] E. Mediavilla[3] and E. Battaner[2]

[1]*Dpto. de Astrofísica y CC. de la Atmósfera, Universidad Complutense de Madrid, Spain*
[2]*Dpto. Física Teórica y del Cosmos, Universidad de Granada, Spain*
[3]*Instituto de Astrofísica de Canarias, Tenerife, Spain*

Accepted 2007 June 13. Received 2007 May 9; in original form 2006 December 21

ABSTRACT

We analyse new integral-field spectroscopy of the inner region (central 2.5 kpc) of the spiral galaxy NGC 4321 to study the peculiar kinematics of this region. Fourier analysis of the velocity residuals obtained by subtracting an axisymmetric rotation model from the Hα velocity field indicates that the distortions are *global* features generated by an $m = 2$ perturbation of the gravitational potential which can be explained by the nuclear bar. This bar has been previously observed in the near-infrared but not in the optical continuum dominated by star formation. We detect the optical counterpart of this bar in the 2D distribution of the old stellar population (inferred from the equivalent width map of the stellar absorption lines). We apply the Tremaine–Weinberg method to the stellar velocity field to calculate the pattern speed of the inner bar, obtaining a value of $\Omega_{\rm b} = 160 \pm 70\,{\rm km\,s^{-1}\,kpc^{-1}}$. This value is considerably larger than the one obtained when a simple bar model is considered. However, the uncertainties in the pattern speed determination prevent us from giving support to alternative scenarios.

Key words: galaxies: individual: NGC 4321 – galaxies: kinematics and dynamics.

1 INTRODUCTION

Departures from regular rotation, such as winds, elongated orbits or streaming motions, provide very relevant information about the dynamics and history of galaxies. To identify kinematical distortions and to infer how they relate to the gravitational potential, different techniques such as velocity field fitting or Fourier analysis can be used. However, to obtain reliable results these tools must be used in combination with 2D kinematical data of good spatial resolution. Integral-field spectroscopy (IFS) is an observational technique especially suited for kinematical studies that can be applied to nearby galaxies, such as M100 (NGC 4321), to obtain velocity maps with detailed spatial information.

The inner region of NGC 4321 has been extensively studied at different wavelengths. Optical (Pierce 1986), Hα, near-infrared (NIR) (Knapen et al. 1995a,b) and CO studies (Rand 1995; Sakamoto et al. 1995; Sempere & García-Burillo 1997) have revealed some interesting irregular features. On the one hand, the inner region of this galaxy shows a peculiar morphology that is quite different in the optical and the NIR. In the optical, the structure is dominated by two spiral arms (broad-band) and an oval-shaped region of enhanced star formation (Hα, Hβ), while the NIR shows an inner bar aligned with the large-scale stellar bar and a pair of small arms emerging from its ends (Knapen et al. 1995a,b). Whether there is a single bar or two nested bars that just happen to be aligned has been a greatly debated issue (Knapen et al. 1995b, 2000; García-Burillo et al. 1998; Wada, Sakamoto & Minezaki 1998). On the other hand, Knapen et al. (2000) found non-circular motions from Hα data, and interpreted them as the kinematical signatures of gas streaming along the inner part of the bar, and of density-wave streaming motions across a two-armed minispiral. Relevant pattern speeds of this galaxy have been measured at larger scale by different methods (Canzian & Allen 1997; Sempere et al. 1995; Hernández et al. 2005, and references therein). Recently, Allard, Peletier & Knapen (2005a) have analysed the inner region of NGC 4321 from IFS observations obtained with SAURON. They focus on the star formation ring, which they confirm to be formed by young stars, but find a low gas velocity dispersion compared to its surroundings.

In this paper we present new IFS (covering a large wavelength range in the optical) obtained with *INTEGRAL*, a system of exchanging fibre bundles at the William Herschel Telescope (WHT) suited for this kind of study (García-Lorenzo, Arribas & Mediavilla 2001; Battaner et al. 2003; Mediavilla et al. 2005). We use the stellar and ionized gas velocity fields to analyse the symmetries of the departures from pure rotation and to estimate the nuclear bar pattern speed by means of the Tremaine & Weinberg (1984) method. These studies will be used to relate the morphological and kinematical distortions observed in the inner 2.5 kpc with the gravitational potential of the nuclear bar.

⋆E-mail: acm@astrax.fis.ucm.es

Table 1. M100 main properties.

Name	M100
Type	SAB(s)bc LINER-H II
RA (J2000)	$12^h22^m54\overset{s}{.}9$
Dec. (J2000)	15° 49′ 20″
Inclination	30°
PA	151° ± 3°
Total magnitude (*B*)	10.05 mag
Systemic velocity (optical)	1567 ± 7 km s^{-1}
Distance	16.1 Mpc
Linear scale	78 pc arcsec^{-1}

NGC 4321 has a very accurately (Cepheid) measured distance of 16.1 Mpc (Ferrarese et al. 1996) which corresponds to 78 pc arcsec^{-1} on the plane on the sky. We use this value throughout this work.

The main properties of M100 are summarized in Table 1.

2 OBSERVATIONS AND DATA REDUCTION

The data analysed in this article were obtained on 2002 March 16 at the Observatorio del Roque de los Muchachos on the island of La Palma with the fibre system *INTEGRAL* (Arribas et al. 1998) in combination with the fibre spectrograph WYFFOS at the WHT (Bingham et al. 1994). The weather conditions during this night were fairly good, with a seeing of about 1.3 arcsec. The data discussed in this paper were obtained with *INTEGRAL* standard bundles #3 and #2. The WYFFOS spectrograph was equipped with a 1200 groove mm^{-1} grating centred on 6247 Å. The spectral resolution was 4.8 Å ($R \approx 1300$) for SB3 and 2.8 Å ($R \approx 2200$) for SB2 fibre bundles. *INTEGRAL* + WYFFOS allow us to observe a large (compared with other IFS systems) spectral range (5600–6850 Å) that, in addition to Hα, also contains the high excitation [N II]$\lambda\lambda$6548, 6584 and [S II]$\lambda\lambda$6716, 6731, emission lines and the NaD $\lambda\lambda$5890, 5896 absorption features (see Fig. 1a) not included in previous IFS studies. With this configuration, and pointing to the centre of NGC 4321, we took three exposures of 1200 s each during the night.

The data reduction of fibre-based 2D spectroscopy (e.g. Arribas, Mediavilla & Rasilla 1991; Mediavilla, Arribas & Rasilla 1992) consists of two main steps: (i) basic reduction of the spectra (i.e. bias, flat-fielding, extraction, wavelength calibration, etc.) and (ii) generation of maps of spectral features (e.g. line intensity, velocity fields, etc.) from the spectra. Step (i) was performed in the IRAF environment following standard procedures. We obtained typical wavelength calibration errors of 0.15 Å, which give velocity uncertainties of ±7 km s^{-1} for Hα. For step (ii) we have developed our own software packages. In particular we transform an ASCII file with the actual position of the fibres and the spectral feature corresponding to each fibre into a regularly spaced rectangular grid. In this way we build up images of 33 × 29 pixels for SB3 bundle, and 45 × 34 pixels for SB2, with a scale of ∼0.95 arcsec pixel^{-1}, and 0.35 arcsec pixel^{-1} for SB3 and SB2 fibre bundles, respectively. The resulting images are therefore of sizes 31.35 × 27.55 arcsec^2 for SB3 and 15.75 × 11.9 arcsec^2 for SB2. These images can be treated with standard astronomical software.

3 RESULTS

3.1 Nuclear spectrum

The stellar population in the central region of NGC 4321 has been carefully analysed by Sarzi et al. (2005). They estimate an average age of 1 Gyr at solar or supersolar metallicities, with only a marginal improvement in the results for supersolar metallicities. We therefore use a synthetic stellar population of 1 Gyr with solar metallicity as a template for the stellar absorption feature analysis. We have used the synthetic population by Delgado et al. (2005), which covers the observed wavelength range at a very high spectral resolution (0.3 Å). This range includes the strong NaD line that might be affected by interstellar absorption. We thus exclude the wavelength range of NaD from the fitting, obtaining a template that reproduces very well the observed absorption features, except the NaD line, which exhibits strong interstellar contamination. The difference between the nuclear spectrum and the template shows that the interstellar contribution is blueshifted (see Fig. 1b). This is a notable result, since blueshifted velocity components in this feature unambiguously indicate the presence of outflowing gas,

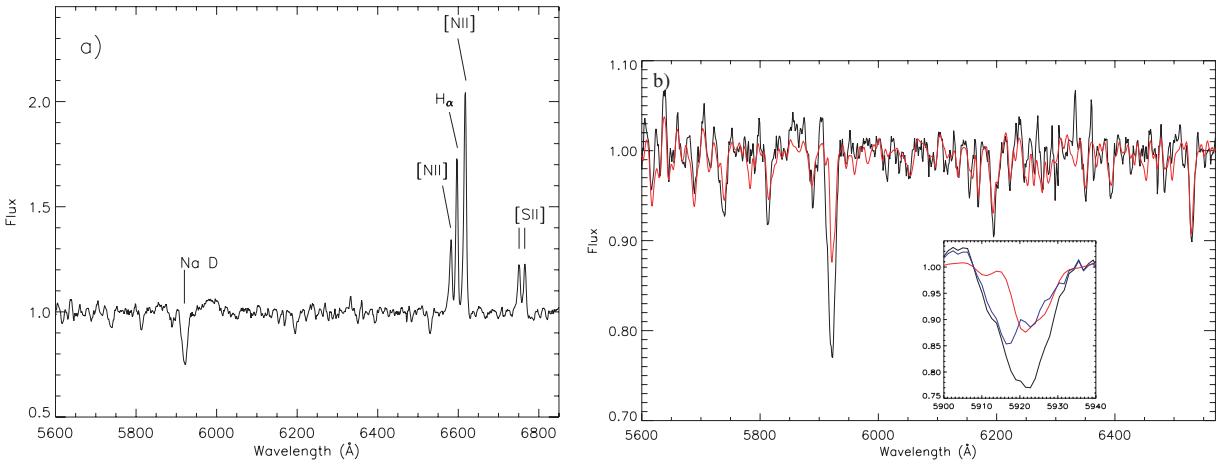

Figure 1. (a) Nuclear spectrum (fibre #68 in bundle SB3) of NGC 4321 in the range 5600–6850 Å showing the most important absorption and emission lines. (b) Nuclear spectrum for the SB3 fibre bundle with the stellar template plotted on top in red line. This template is used with the XCSAO task to derive the stellar velocity field using the cross-correlation technique in the wavelength range 5600–6560 Å. The inner panel shows in detail the fit of the NaD absorption doublet (red line) and the residuals (blue line).

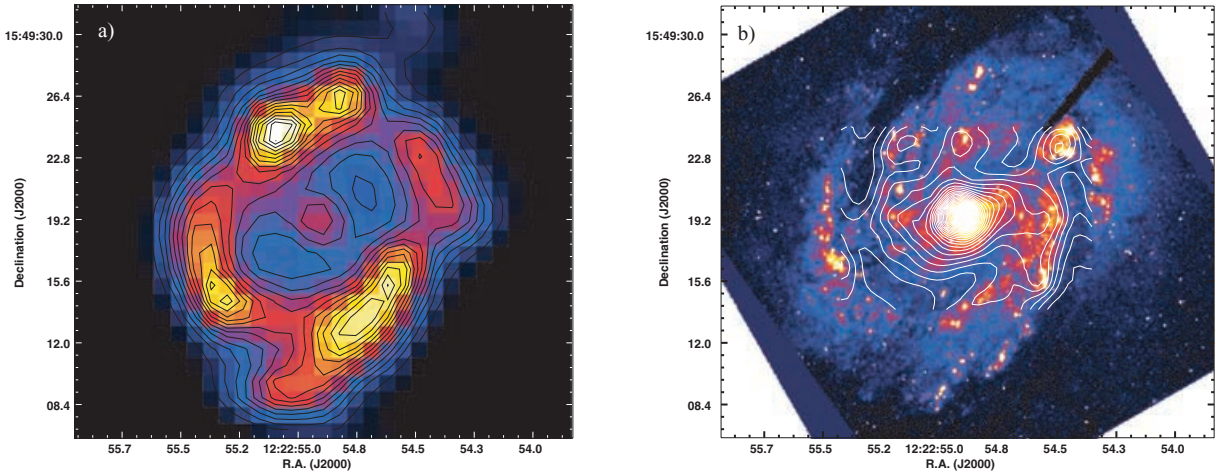

Figure 2. (a) Hα intensity map computed for the SB3 fibre bundle. The Hα emission is distributed in a nucleus and an oval-shaped ring. (b) *HST*/ACS (F555W) image of NGC 4321 with white contours overlaid from the continuum map computed for the SB2 fibre bundle.

as demonstrated in previous studies (see Rupke, Veilleux & Sanders 2005, and references therein).

3.2 Hα maps

To obtain the intensity and velocity maps for the ionized gas we fit a single Gaussian to the Hα emission line after subtracting the stellar contribution from each spectrum. Absorption correction is in general not very important except at the nucleus. According to the Hα intensity map (see Fig. 2a), the emission is distributed in a nucleus and an oval-shaped ring (Knapen et al. 2000; Allard et al. 2005a), where several H II regions can be distinguished.

The Hα velocity field map is computed with the combined information from the SB2 and SB3 fibre bundles (see Fig. 3a). Our velocity map looks quite similar to the one published by Knapen et al. (2000). It essentially shows a basic rotational pattern significantly distorted by the effect of the inner bar and spiral arm structures. In Fig. 3(b) we overplot the ionized gas velocity contours on the *Hubble Space Telescope* (*HST*)/ACS (F555W) image. In this figure, the two regions with clear departures from axisymmetric circular rotation stand out clearly. The innermost region shows a clear twist in the kinematic axes due to the influence of the inner bar. Further out, the deviations follow the spiral arms.

3.3 Stellar maps

Cross-correlation of the spectra is performed in the 5600–6560 Å wavelength range with the XCSAO task from the IRAF package. We have excluded in the cross-correlation wavelength ranges around the [O I]$\lambda\lambda$6300, 6363 lines to avoid residual sky emission contamination and a wavelength range around the NaD feature (for the reasons mentioned above). The stellar velocity uncertainties ranges from 15 km s^{-1} (inner regions) to 35 km s^{-1} (outer regions). The resulting stellar velocity field is shown in Fig. 4(a). It looks very similar to the results published by Allard, Peletier & Knapen (2005b). Although noisier than the gas velocity field, it shows a stellar rotation pattern that is more regular than the velocity pattern of the ionized gas. It shows some distortions in the bar region although not as strong as in the case of the gas. The strongest deviations from circular rotation in the map take place at two spots in the spiral arms. They are located roughly symmetrically with respect to the galactic centre with a position angle (PA) of about 45° from the major axis (nearly perpendicular to the bar PA), coincident with the highest density regions of the CO map by Sakamoto et al. (1995). This supports the role of the nuclear bar in explaining the complex kinematics and morphology in the innermost region of NGC 4321. This issue, and the question of whether the nuclear bar is part of the large-scale one present in this galaxy or a separated structure (see Hernández et al. 2005, for a review) will be addressed in Section 4.3.

The stellar continuum map shows very similar features to the broad-band *HST*/ACS (F555W) image although at a lower spatial resolution (see Fig. 2b). In this map we can distinguish the nucleus emission from which a spiral structure is coming out in the south-west direction and a fainter one at the north-east direction. Dust structures at the inner rims of the arms are also clearly seen in the *INTEGRAL* continuum map (see also Knapen et al. 1995a,b). The brightest regions in this map trace stellar formation regions, of which is particularly clear the bright region surrounded by dust in the north-west of the nucleus.

We have also calculated maps for the strength and equivalent width (EW) of the stellar absorption lines from the fittings of the template to the spectra obtained during the cross-correlation procedure (see previous section). It should be kept in mind that we have used the same single-age, single-metallicity population template for the whole map, and that therefore the maps for the intensities and EWs of all the stellar absorption lines are proportional. This is obviously an oversimplification, as we know there will be variations in stellar populations throughout the field of view, but a thorough analysis of the stellar populations is beyond the scope of this paper, and these maps are intended only to be a tracer of the global stellar mass content of the galaxy. Note that we have obtained a map normalized (according to the template) to the NaD line absorptions, which are the strongest ones in the wavelength range studied. This NaD map is therefore free from interstellar contamination.

Fig. 5 shows the contours of the EW of the stellar NaD line on top of the WHT K_s image from Knapen et al. (2003). The isolevels of the EW in the innermost region are elongated with a PA very close

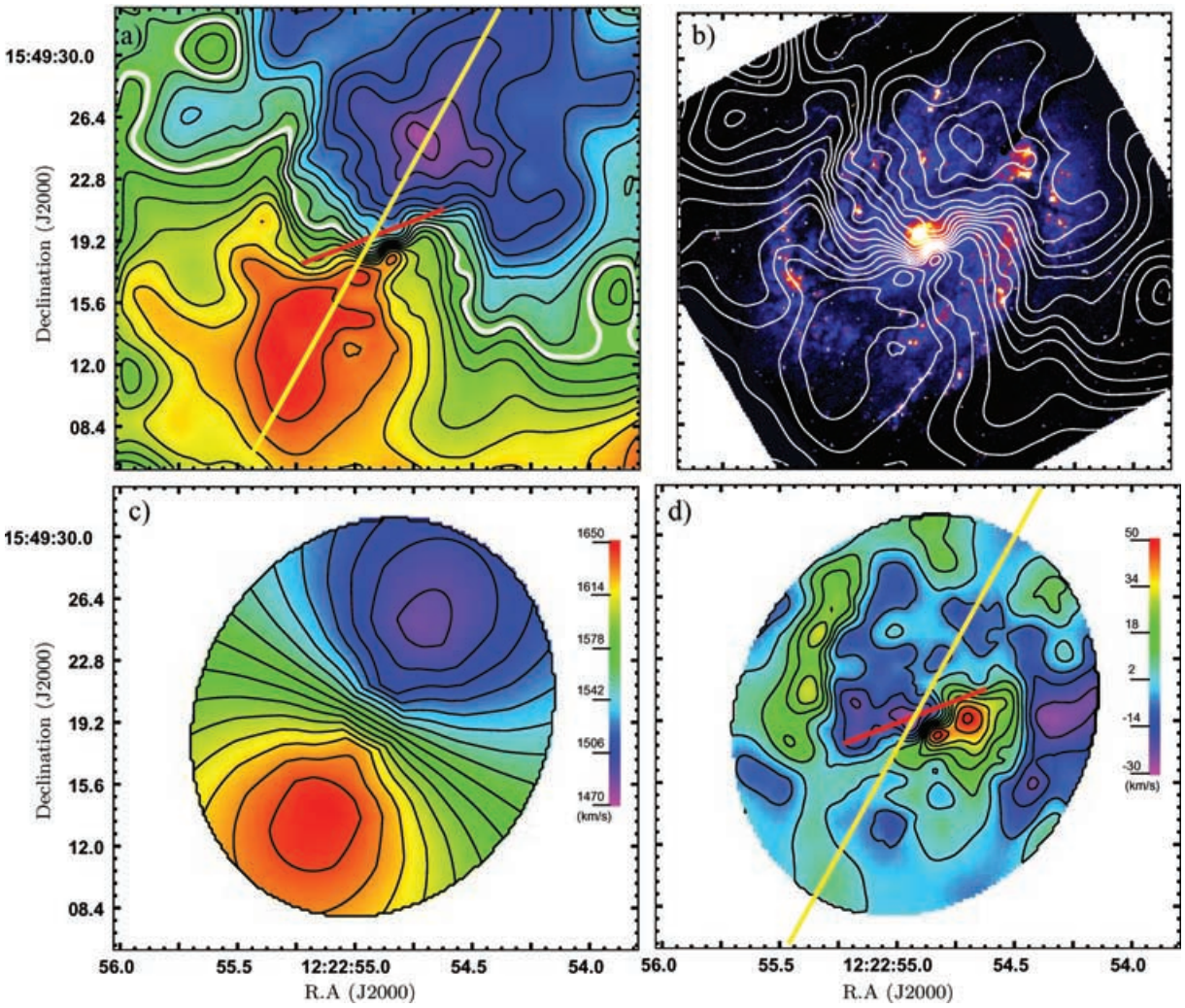

Figure 3. (a) Hα velocity map computed with the information from the SB2 and SB3 fibre bundles. Contour levels range from 1470 to 1650 km s^{-1} in steps of 10 km s^{-1}. The thick white contour indicates the systemic velocity at 1567 km s^{-1}. Figs (a) and (c) share the same scale colour bar. (b) *HST*/ACS (F555W) image of NGC 4321 with white contours of Hα velocity field overlaid. (c) Model velocity map with fixed PA (see text). (d) Map of residual velocities derived by subtracting the model velocity field (c) from the observed velocity map (a). Contour levels: from -30 to 50 km s^{-1} in steps of 8 km s^{-1}. Yellow and red lines show the PA of the galaxy (PA = 151°) and the inner stellar bar (PA = 111°), respectively.

to the 111° quoted by Knapen et al. (1995a) for the inner bar. The extent of the bar does also roughly agree with the 9 arcsec proposed by Knapen et al. (1995a). Although this is not completely surprising (as the EW is expected to be somewhat less affected by dust than continuum or broad-band maps), it clearly shows that the EW is a good tracer of the old population responsible for the absorption features. The two well-known IR knots K1 and K2 (Knapen et al. 1995a) do not show up in the EW map and in fact correspond to minima on it (see Fig. 5). These knots are known to be regions of powerful recent star formation (Wozniak et al. 1998; Ryder & Knapen 1999) and are therefore very bright because of the contribution of young stars, but not necessarily rich in old stars responsible for the absorption features contributing to the EW. Although the spectra are smeared by poor angular resolution, we have been able to detect, for the first time, the (otherwise hidden) inner bar through the study of absorption spectral features characteristic of old stars. We would like to point out that, the K_s-band image shows very little hint of the spiral arms (Knapen et al. 1995a,b). This fact indicates that the mass distribution is quite axisymmetric at radii larger than ≈6 arcsec.

4 DISCUSSION

4.1 Residual velocity field of the ionized gas

Departures from circular motion are better addressed through residual velocity analysis. We therefore start by deriving a pure rotation model by fitting tilted rings to the observed velocity field (Begeman 1989). This is a standard procedure for which the galaxy is divided into concentric elliptical annuli where each annulus is characterized by the inclination angle (i), the position angle of the major axis (PA), the rotational velocity (v_c), the systemic velocity of the galaxy (v_{sys}) and the coordinates of the centre of each annulus (x_c, y_c). These parameters are fitted following a least-squares algorithm. We have used the task ROTCUR from the data reduction software package GIPSY (Groningen Image Processing SYstem) for this purpose.

We take the kinematical centre at the position of the nuclear source at our highest available spatial resolution. This position matches, within the resolution limits, the position of the brightest spot in the *HST* image. We fix the inclination to a value of 30° (Knapen, Pérez-Ramírez & Laine 2002). The systemic velocity is

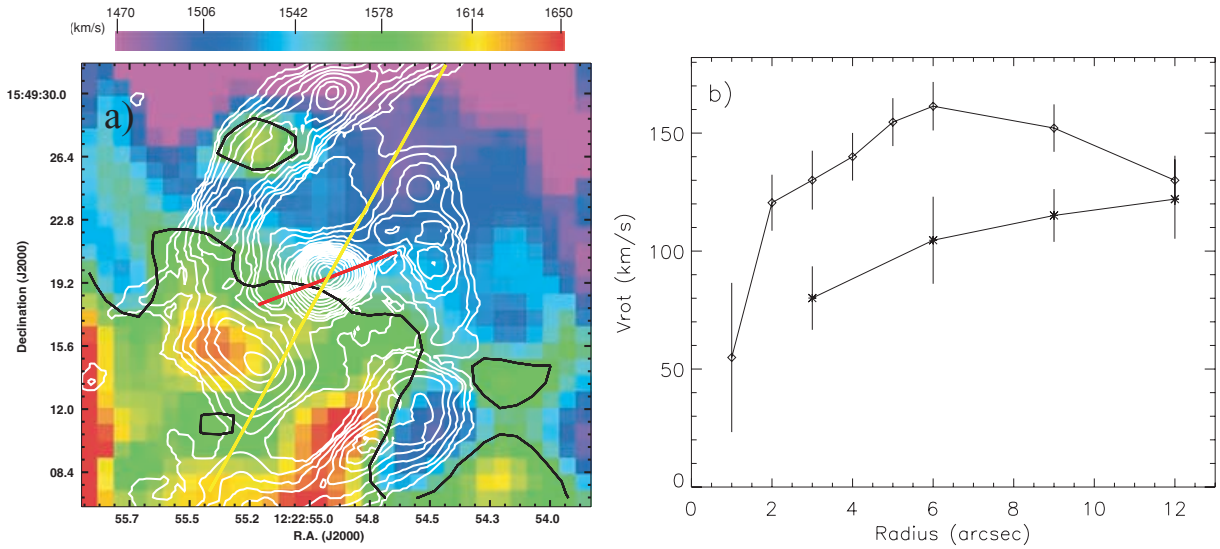

Figure 4. (a) Stellar velocity field for the SB3 fibre bundle. Velocities range from 1470 to 1650 km s^{-1}. The thick black contour indicates the systemic velocity at 1567 km s^{-1}. Yellow and red lines show the PA of the galaxy (PA = 151°) and the inner stellar bar (PA = 111°), respectively. Contours of the CO emission are overplotted in white. (b) Stellar (star symbols) and Hα (diamond symbols) rotation curves of the inner disc of NGC 4321 derived up to 12 arcsec (≈1 kpc) from the galactic centre.

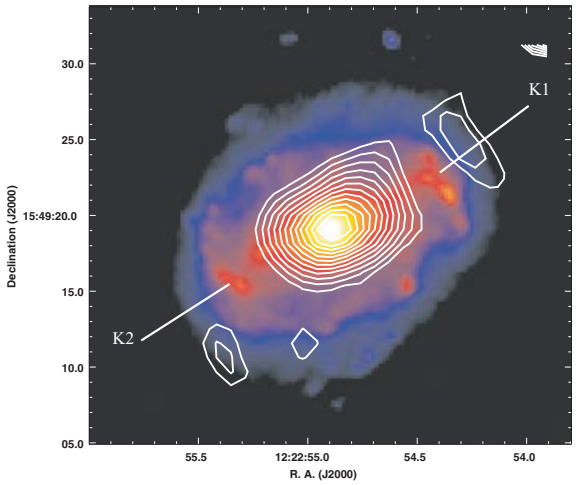

Figure 5. IR (K_s) image of NGC 4321 from (Knapen et al. 2003) with contours of the NaD EW for the SB3 fibre bundle. Contour levels range from 0.75 to 1.3 Å in steps of 0.05 Å. IR knots K1 and K2 (Knapen et al. 1995a) are marked.

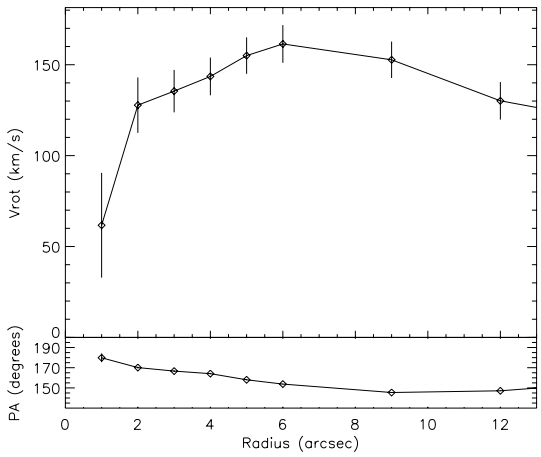

Figure 6. Hα rotation curve of the inner disc of NGC 4321 derived up to 12 arcsec (≈1 kpc) from the galactic centre. The lower panel shows variations of PA with radius.

calculated as the average value of the outermost rings. We obtain a value of 1567 ± 7 km s^{-1} . With these values fixed, we perform a fit leaving the PA and the rotational velocity of each ring as free parameters. The results are shown in Fig. 6. The error bars in the rotation curves of Figs 6 and 4(b) are calculated from the difference in the rotation curves calculated for the approaching and receding sides of the galaxy and the error in the velocity determination, which have been added quadratically.

The rotation curve obtained shows a very similar behaviour to previous observations (Sakamoto et al. 1995; Knapen et al. 2000). Our values are in fact somewhat lower than those reported by Knapen et al. (2000), but in good agreement with CO observations by Sakamoto et al. (1995). Although, as usual, the inner region provides the most uncertain determination of the rotation curve, we have checked that rotations curves calculated for the maps at the two available resolutions (SB2 and SB3 fibre bundles) give an excellent agreement for the values of the rotational velocity in the overlapping regions. Resolution effects will therefore not be too relevant in the shape of the inner rotation curve.

The rotation curve shows a very steep rise in the inner 3 arcsec, reaching values of 135 km s^{-1}. The velocity reaches a maximum of about 160 km s^{-1} at 6 arcsec (470 pc) and then declines smoothly to a value of 130 km s^{-1} in the outermost ring at 12 arcsec (≈1 kpc).

To investigate the non-circular motions in the galaxy disc we compute the residual velocity map. We would like to minimize the effect of non-circular motions being absorbed in the rotational model. We use for this purpose a rotational model with a fixed PA (= 151° ± 3°, which is the average of the PA values corresponding to the outermost rings). In this way, most of the information on non-axisymmetric components is kept in the residual velocity. Of course, deviations from circular rotation that take place along or near the major axis in a symmetric way (on both the approaching and

the receding sides) will most probably be absorbed in the rotation curve shape. There is little hope of disentangling the non-circular and circular components along the major axis, and therefore we adopt this as the best possible solution. The calculated axisymmetric rotational model is displayed in Fig. 3(c). Subtracting this model from the observed velocity field, we obtain the residual velocity map for NGC 4321 which is shown in Fig. 3(d).

Three regions can be clearly identified in the residual velocity map. (i) A blueshifted nuclear region that shows blue residuals of about $-25\,\mathrm{km\,s^{-1}}$. We would like to point out that although the rotation curve is quite uncertain in the innermost region, th e existence of these blue residuals in the nuclear region does mostly depend on the position of the kinematic centre and on the systemic velocity, which are both pretty well constrained by the observations. This fact suggests the existence of an outflow in this region. (ii) A second region, farther out up to radii of about 6 arcsec, that shows a clear signature of influence of the nuclear bar (whose PA and size are shown in Fig. 3d by the red line). The map shows residuals of nearly $50\,\mathrm{km\,s^{-1}}$ on the west side and of $-25\,\mathrm{km\,s^{-1}}$ on the east side. These are the zones where orbits tend to align with the bar potential. The symmetric shape of this region above and below the bar is quite remarkable. (iii) At larger radii ($r > 6$ arcsec) the residual map shows clear signatures of the presence of the spiral arms with values of 30 km s^{-1} for the northern arm and $-25\,\mathrm{km\,s^{-1}}$ for the southern arm. The northern arm is more clearly depicted than the southern one. In fact, as can be seen in Fig. 7(a), the residuals for the northern arm nicely match the position of the molecular gas from the CO map by Sakamoto et al. (1995). The southern arm is somewhat displaced from the position where the highest residuals are found. The residual velocities along the arms seem to vanish as they approach the major axis, although, as we have mentioned before, it is very likely that a large fraction of the non-circular motions has been absorbed in the shape of the rotation curve. The latter two of the three regions have already been identified by Knapen et al. (2000). In Section 4.2 we perform a Fourier analysis of the ionized gas kinematics to study the relationship of these regions with the gravitational potential.

It is worth noting that the highest Hα intensity spots take place in regions of low residual velocities (see also Zurita et al. 2004). In fact, in the case of NGC 4321, the Hα ring of star formation actually lies in the transition region between the bar and arm regions (with a radius of about 6 arcsec) with very low residual velocities. It is indeed very likely that both facts (high Hα intensity and low residual velocities) are closely related and star formation takes place in a *kinematically quiet* region.

A careful look at these residuals also reveals that the highest velocity gradients (which trace shocked gas regions) take place at the inner rim of the spiral arms and around the nucleus of the galaxy (at its far side). This is better illustrated if we calculate the gradient of the residual velocity field. We have used the Roberts (Roberts 1965) operator to compute the 2D spatial gradient measurement on the residual velocity field. The residual velocity gradient contours are shown on top of an unsharp-masked *HST* image of NGC 4321 in Fig. 7(b). It is quite impressive how the shocked gas traced by the high gradient matches very well the location of the dust lanes along the inner rim of the arms (particularly for the northern arm). This indicates that the spiral arms are very probably formed by hydrodynamic shocks originated by gas orbit crowding at a resonance of the bar potential (as the mass distribution as traced by the NIR light shows no relevant overdensities at these locations). This coincidence of the dust location with high velocity gradients was also found and studied in detail for NGC 1530 by Zurita et al. (2004).

The nuclear velocity gradient, although mixed with some bar-generated shocks, may also be understood in the context of the presence of an outflow in the nuclear region. If the approaching side of an outflow (more likely to be detected than the receding one, located behind the galactic disc) produces a region of shocked gas over the nuclear region, this would be seen in projection somewhat displaced along the minor axis on the far side of the disc. Additional indications of an outflow can be found in the morphology of the emission line profiles of the innermost region spectra that show blue shoulders and blue wings, especially in the high excitation lines

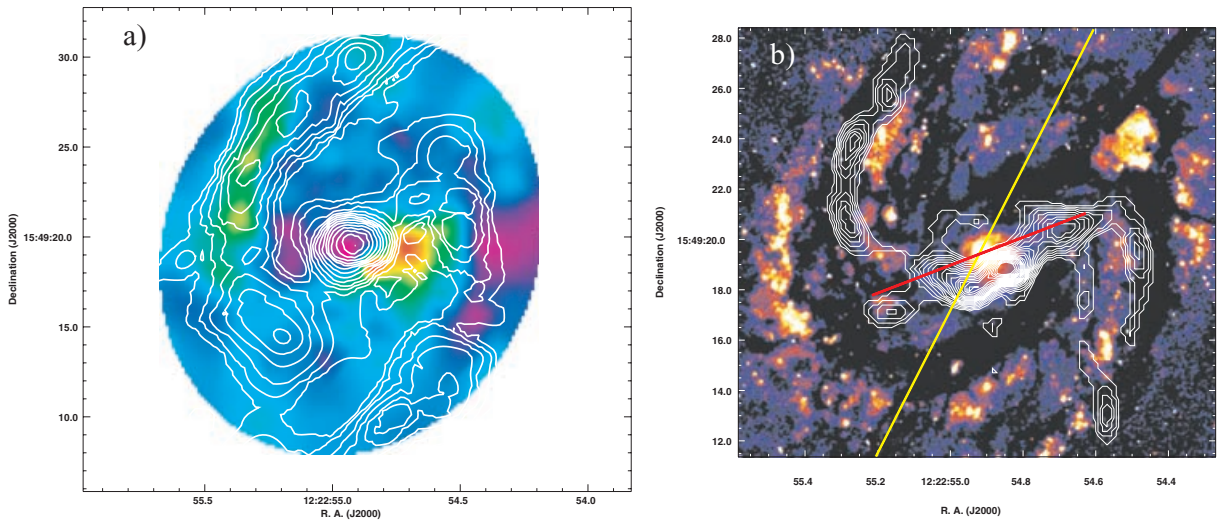

Figure 7. (a) The residual velocities (colour image) nicely match the position of the molecular gas from the CO emission shown in white contours. (b) *HST*/ACS (F555W) unsharp-masked image of NGC 4321 with residual velocity gradient contours overlaid. Yellow and red lines show the PA of the galaxy (PA = 151°) and the inner stellar bar (PA = 111°), respectively.

([N II], [S II]). In other galaxies (see e.g. Arribas & Mediavilla 1993, 1994), these features are an evidence of streaming gas. Finally, the existence of a nuclear outflow is also supported by the blueshifted interstellar contamination of the NaD absorption (see Fig. 1b), very common in superwind galaxies (Heckman et al. 2000).

4.2 Fourier analysis of the residual velocity field

We would like to go one step further in the analysis of the residual velocity field of NGC 4321. One of the most striking features of the residual velocity map is its great degree of symmetry. Knapen et al. (1995a) already noted that the *K*-band image of the nuclear region of NGC 4321 presented a high degree of symmetry. They performed a decomposition of the symmetric and antisymmetric components of this image, finding that an impressive 95 per cent of the flux is emitted in the symmetric component. If, as expected, the *K*-band image is a good tracer of the mass density and hence of the potential, it is reasonable also to expect a high degree of symmetry in the kinematical signature of such a potential. We have therefore performed the same kind of decomposition in our residual velocity field. The result of such a procedure is shown in Fig. 8(a), where the residual velocity map is shown in colours with regions of symmetry and antisymmetry dominance plotted on white and black contours, respectively. The three distinctive regions mentioned in Section 4.1 now stand out more clearly. The central region is the only one that shows a relevant symmetric dominance (with blueshifted velocities) while the bar and arm influence zones are regions of antisymmetric dominance. The rest of the map does not show any definite symmetry.

It is not surprising that most of the residuals belong to the antisymmetric component. As Knapen et al. (1995b) showed, there is a clear $m = 2$ component in the potential generated by the nuclear bar. Canzian (1993), and later Schoenmakers, Franx & de Zeeuw (1997) in an analytical way, showed that a perturbation of harmonic number, m, in the potential shall generate $m - 1$ and $m + 1$ signatures in the velocity field (dominating inside and outside corotation, respectively).

The antisymmetric component is dominated by an harmonic $m = 1$ mode, while the symmetric component is contributed by a combination of even modes (mostly $m = 0$). To show this in a clearer way, we have also performed a Fourier analysis of the residual velocity field. The residual velocity field is decomposed into its Fourier components in rings of different radii. Each ring is therefore characterized by the amplitude $F_m(R)$ and phase $\phi_m(R)$ of each Fourier component m. The results are shown for the first four modes in Fig. 8(b). The amplitude of modes $m > 4$ is negligible at all radii. The three regions of definite symmetry coincide with the regions of high residuals already mentioned: $m = 0$ dominance for the nuclear region, $m = 1$ for the bar (with a very constant phase angle and spiral arms (with a phase angle varying with radius). The $m = 3$ mode is second in importance in the bar and spiral arms regions.

In our case, if the bar $m = 2$ perturbation to the potential is responsible for the deviations from circular rotation, we expect, according to Schoenmakers et al. (1997) a strong $m = 1$ signature (with a secondary $m = 3$) in the residual velocity field (as we are inside the corotation radius and $\Omega_b < \Omega$). This is exactly what is observed in our data for NGC 4321. Although a spiral structure is also a $m = 2$ distortion and would therefore produce $m - 1 = 1$ and $m + 1 = 3$ signatures in the velocity field, we strongly favour the bar scenario. The constancy of the phase angle of the $m - 1 = 1$ in the innermost region (see Fig. 9) clearly indicates a perturbation with a constant PA, as one would expect from a bar. Moreover, the NIR photometry of NGC 4321 clearly shows the nuclear bar, but no trace of spiral arms in the mass distribution.

The Fourier analysis therefore shows clearly that the velocity residuals are not local perturbations but *global* modes (due to the high degree of symmetry) generated by the $m = 2$ potential perturbation of the nuclear bar. The spiral arms are also generated by the bar potential. The generation of the spiral arms is most probably caused by shocks originated by gas orbit crowding at a resonance (see e.g. Sakamoto et al. 1995).

4.3 Stellar rotation curve. Application of the Tremaine–Weinberg method

We calculate the stellar rotation curve from the stellar velocity map (see Fig. 4a) using the same method employed for the ionized gas. We fix the position of the centre, inclination, PA and systemic velocity to the values used for the ionized gas, and leave the circular velocity as the only free parameter in the fit. Fig. 4(a) may give the wrong impression of an offset between the kinematical and photometrical centres. This is due to a combination of facts, the most important being that the systemic velocity plotted in Fig. 4(a) is the one calculated for the gas (which is used in the rotation

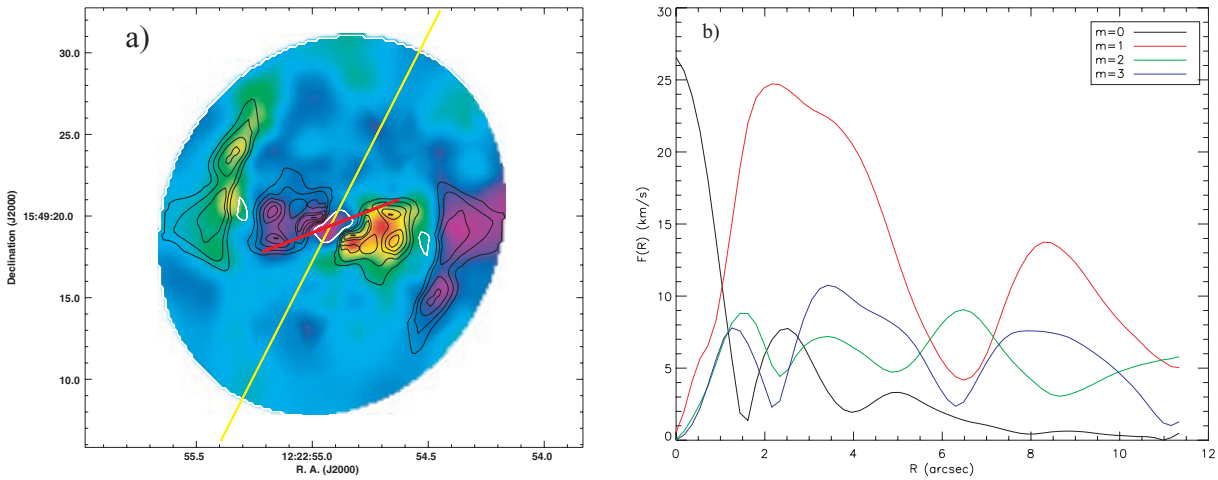

Figure 8. (a) Residual velocity field (colour image) with the symmetric and antisymmetric dominance regions overplotted on white and black contours, respectively. (b) Radial variation in amplitude of the Fourier modes of the residual velocity field. We show the results for the first four modes.

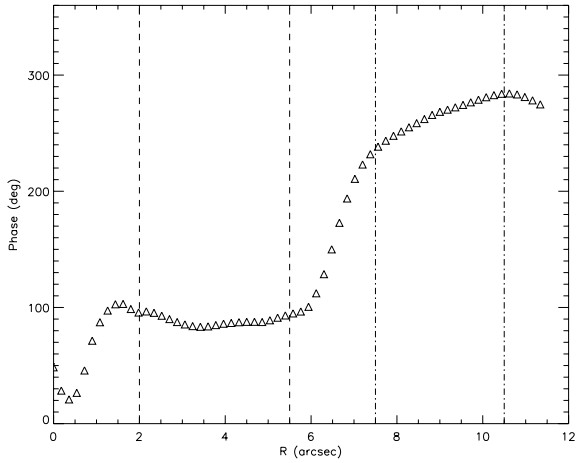

Figure 9. Phase angle for $m = 1$ mode in the Fourier analysis of the gas residual velocity field. The bar region (between dashed vertical lines) shows a constant phase and the spiral arms region (between dot–dashed vertical lines) shows a phase varying with radius.

model). The systemic velocity computed from the stellar velocity field would give a slightly lower value, resulting in an isovelocity contour closer to the photometrical centre. We have chosen to keep the determination of the systemic velocity from the ionized gas [with a much higher signal-to-noise ratio (S/N)] despite this spurious effect.

The resulting stellar rotation curve is shown in Fig. 4(b). It rises more slowly in the innermost region but shows a very similar behaviour to the gaseous rotation curve. The values of the stellar rotational velocity are always smaller than the gaseous ones. Qualitatively, this is to be expected owing to the stars' asymmetric drift.

The pattern speed of the bar in NGC 4321 and the existence of two nested bars or a single bar have been a much debated issue (see Hernández et al. 2005, for a review). In any case, what seems to be clear is that there are several relevant pattern speeds in NGC 4321. Most observational determinations (see Hernández et al. 2005, and references therein) seem to agree on a value of $\Omega_p \approx 20{-}35\,\mathrm{km\,s^{-1}\,kpc^{-1}}$ for the outer spiral arms. The discrepancies arise in the inner region and over whether the large-scale bar and the nuclear bar are the same or different structures. Comparison of numerical simulations with observations has left two surviving alternatives. On one side Wada et al. (1998) and Knapen et al. (2000) favour a single bar scenario in which the pattern speed of the bar is $\Omega_b \approx 70\,\mathrm{km\,s^{-1}\,kpc^{-1}}$. If the large-scale bar has to rotate at such a high speed, this scenario seems to contradict the above-mentioned fact that most observational studies determine a much lower pattern speed for the outer regions (where both the large-scale bar and spiral arms coexist). The alternative model proposed by García-Burillo et al. (1998) consists of two nested bars with different (although closely linked) pattern speeds. Their best solution provides fast and slow pattern speeds of $\Omega_f = 160\,\mathrm{km\,s^{-1}\,kpc^{-1}}$ and $\Omega_s = 23\,\mathrm{km\,s^{-1}\,kpc^{-1}}$, respectively. This alternative has the virtue of being able to drive gas inwards thanks to the fast mode (as in the single bar model) in the inner region while keeping the observed slow mode at large radii.

The best observational determination of the pattern speeds of structures in galactic discs is provided by the method proposed by Tremaine & Weinberg (1984) (hereafter TW). This method does not rely on any particular theory or numerical simulations. It relies exclusively on the continuity equation. In a Cartesian coordinate system (x, y) where the x- and y-axes are aligned with the galaxy's major and minor axis, respectively, they showed that if one can find observationally a tracer of the mass density and the velocity of a galactic component that satisfies the continuity equation, then the underlying pattern speed can be calculated from this observational information as

$$\Omega_p = \frac{1}{\sin i}\frac{\int_{-\infty}^{\infty}\Sigma(x)[v_{los}(x) - v_{sys}]\,dx}{\int_{-\infty}^{\infty}\Sigma(x)(x - x_c)\,dx} = \frac{1}{\sin i}\frac{\langle V_{los}\rangle}{\langle X\rangle}, \quad (1)$$

where $\Sigma(x)$ is the observed intensity (assumed to be proportional to the surface mass density), $v_{los}(x)$ is the line of sight velocity, v_{sys} is the systemic velocity and x_c is the x coordinate of the centre. The integrals are performed along slits or slices parallel to the major axis direction. TW also pointed out the convenience of using an odd weighting function in y by using, for example, slits offset by the same amount on both sides of the centre. Merrifield & Kuijken (1995) refined the method by noting that a plot of $\langle V_{los}\rangle$ versus $\langle X\rangle$ provides a combined measurement of the pattern speed using several slits, which is insensitive to errors in the centre position and systemic velocity.

As commented above, the TW method has been applied to several gaseous components, such as Hα (Hernández et al. 2005) or molecular gas (Rand & Wallin 2004). However, it is arguable whether these components satisfy the continuity equation. Stars, particularly old stars, on the contrary, are assumed to survive several cycles around the centre and thus, are expected to satisfy the continuity equation. It is, therefore, interesting to use our stellar velocity field and the strength of a stellar absorption line (as a tracer of the mass surface density) to apply the TW method to the inner region of NGC 4321. The integrals in equation (1) are performed along 21 slits parallel to the major axis and centred on the galaxy centre. The slits are offset by 1 arcsec. The resulting $\langle V_{los}\rangle$ versus $\langle X\rangle$ plot is shown in Fig. 10. The plot shows also a *symmetrized* version by using an odd $\delta(y - y_c) - \delta(y + y_c)$ weighting function in the integrals. The $\langle Y\rangle$ versus $\langle X\rangle$ plot shown in Fig. 11 removes the possible degeneracies between different pattern speeds (see Hernández et al. 2005).

Both fits (for the unweighted and symmetrized data) provide very similar results with a slope value of $\Omega_b = 160 \pm 70\,\mathrm{km\,s^{-1}\,kpc^{-1}}$. The quoted error contains the contribution from uncertainties in the PA. As a cross-check we have also used the K_s IR image of

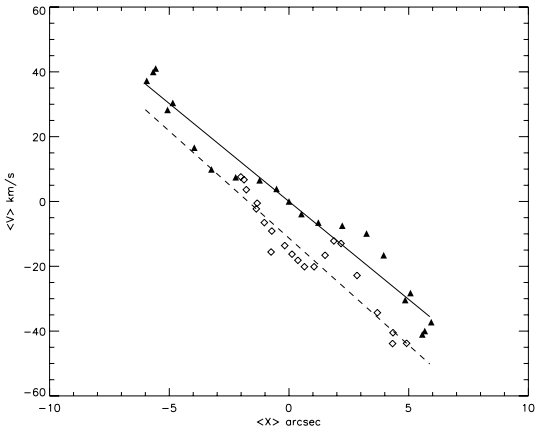

Figure 10. Results of the TW method. This plot shows the results for the unweighted data (empty diamonds) with the best fit (dashed line). The *symmetrized* version is shown in solid triangles with the best fit as a solid line (see text for details). Both fits (for the unweighted and symmetrized data) provide very similar results with in a value of the slope of $\Omega_b = 160 \pm 70\,\mathrm{km\,s^{-1}\,kpc^{-1}}$.

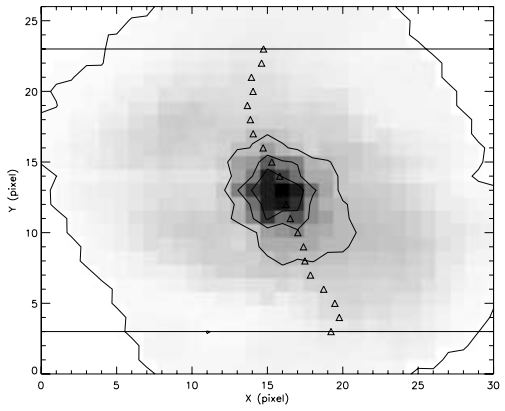

Figure 11. $\langle Y\rangle$ versus $\langle X\rangle$ plot on top of an image of the NaD line strength.

NGC4321 of Knapen et al. (2003) as the mass tracer for the old stars. The results in this case provide a somewhat higher value for Ω_b although compatible with the previous one within the large error bars.

This result is very different from the one associated to the single bar scenario ($\Omega_b \approx 70\,\mathrm{km\,s^{-1}\,kpc^{-1}}$). However, in spite of the numerical coincidence the agreement with the fast mode of the nested bar scenario proposed by García-Burillo et al. (1998), is not conclusive.

A linear trend of the $\langle V_{los}\rangle$ versus $\langle X\rangle$ relationship like the one observed in Fig. 10 is expected for the bar rotation pattern but it is not exclusive of it. In fact, the stellar rotation curve of the inner region of NGC 4321 is approximately described by a linear relationship of about $100 \pm 20\,\mathrm{km\,s^{-1}\,kpc^{-1}}$ between 3 and 12 arcsec. Thus it would be not surprising if the convolution (see equation 1) of the corresponding solid-body like rotating velocity field with a bar of finite width will produce a $\langle V_{los}\rangle$ versus $\langle X\rangle$ linear trend with $\Omega_{rot} \sim 100\,\mathrm{km\,s^{-1}\,kpc^{-1}}$. A direct test repeating the complete procedure to apply the TW method but now to a synthetic velocity field generated with the stellar rotation curve of Fig. 4b yields a value $\Omega_{rot} = 130 \pm 30\,\mathrm{km\,s^{-1}\,kpc^{-1}}$. Thus, Ω_{rot} and $\Omega_b = 160 \pm 70\,\mathrm{km\,s^{-1}\,kpc^{-1}}$ are compatible within errors. In fact, owing to the relative closeness between these two magnitudes (if the two nested bars scenario is correct) a robust determination of Ω_b would need a strong diminution of the errors.

This new determination of the pattern speed has obviously an impact on the location of the important resonances. A higher pattern speed moves most resonances to smaller radii. We have used the linear epicyclic approximation to make an estimation of the resonance location. There are two inner Lindblad resonances located at radii of approximately 6 and 12 arcsec, respectively. The ultraharmonic resonance ($\Omega - \kappa/4 = \Omega_b$) is located at a radius of about 14 arcsec. The star-forming ring seen in Hα is located right inside the outer inner Lindblad resonance and ultraharmonic resonance. Whether this star-forming ring is related to some of these resonances is indeed a possibility, but we cannot be conclusive in this respect. In any case, these values must be considered very cautiously, as they depend critically on the shape of the rotation curve in its innermost region, and on the validity of the linear epicyclic approximation, which is probably a poor one in these regions.

A few words of caution about the determination of the bar pattern speed must be said at this point. The original TW method eliminates some undesired integrals of spatial derivatives by using the fact that the integrals extend to infinity, where the density goes to zero. We obviously cannot fulfil this requirement, as most observations having a limited field of view can not. It is usually assumed that if the intensity is low enough at the borders of the field of view, the method is still usable. As we have seen before, there seems to be evidence that in NGC 4321 there are several speed patterns that are relevant at different radii. If this is the case, integrating along a slit that runs over the two pattern speed regions may contaminate the results of the TW method (for the inner, faster mode), even if we select the appropriate region along the y-axis. In fact, the TW method can be generalized for a continuously varying pattern speed with radius (Merrifield, Rand & Meidt 2006) although its application requires the solution of a Volterra integral equation, which is much more complex and needs very high-quality data over the whole region of interest. It would then be necessary to have high-S/N data of the type presented here covering the whole disc of NGC 4321 to perform such an analysis and to solve this issue definitively.

5 SUMMARY

We have performed a Fourier analysis of the residual velocity field of the ionized gas and determined the stellar bar pattern speed to study the departures from regular rotation and how they relate to the gravitational potential. The main results of this work can be summarized in the following points.

(i) The ionized gas kinematics presents, on top of the galactic rotation, three clearly distinctive regions. (1) A small nuclear region of blueshifted velocities. (2) A bar-dominated region where the residuals originate from the gas orbits aligned with the bar major axis. (3) A region dominated by the streaming motion across two symmetric spiral arms.

(ii) The analysis of the gas kinematical symmetries shows these three regions in a very clear way as regions of dominance of symmetry or antisymmetry, or, alternatively, of $m = 0$ and 1 (secondary $m = 3$) Fourier modes. This is exactly what theory predicts if they are signatures of an $m = 2$ perturbation of the potential. Thus, the outstanding morphological and kinematic perturbations of the circumnuclear region of NGC 4321 present the required (high) degree of symmetry to be explained by the $m = 2$ potential of a bar lying in this region.

(iii) We have detected this (otherwise hidden) bar at optical wavelengths by means of the 2D distribution of the EW of the stellar absorption lines corresponding to the old stellar population. This optical bar matches well the inner bar found in the NIR by Knapen et al. (2003).

(iv) We apply the Tremaine–Weinberg method to the stellar data to estimate the pattern speed of the inner bar. The obtained value of $\Omega_b = 160 \pm 70\,\mathrm{km\,s^{-1}\,kpc^{-1}}$ is very different from the value proposed in the simple bar scenario. However, the uncertainties in the pattern speed determination prevent the confirmation of García-Burillo et al. (1998) results based in the existence of two nested bars.

(v) The nuclear blueshifted region is probably the signature of a nuclear outflow. This is supported by the blueward asymmetry of the emission line profiles and by the presence of a blueshifted interstellar gas component in the NaD absorption.

(vi) Finally, while star formation seems to take place in kinematically quiet regions, the dust location coincides with high velocity gradients.

ACKNOWLEDGMENTS

This paper has been supported by the 'Plan Andaluz de Investigación' (FQM-108) and by the 'Secretaría de Estado de Política

Científica y Tecnológica' (AYA2000-2046-C02-01, AYA2004-08251-C02-02, ESP2004-06870-CO2-02). This research has made use of the NASA/IPAC Extragalactic Database which is operated by the Jet Propulsion Laboratory, California Institute of Technology, under contract with the National Aeronautics and Space Administration. We have used observations made with the NASA/ESA *HST*, obtained from the data archive at the Space Telescope Science Institute (STScI). STScI is operated by the Association of Universities for Research in Astronomy, Inc. under NASA contract NAS 5-26555. J. Jiménez-Vicente acknowledges support from the Consejería de Educación y Ciencia de la Junta de Andalucía. A. Castillo-Morales acknowledges the support from Universidad Complutense de Madrid (AYA2003-01676). We thank J. Knapen and A. Zurita for their help with the astrometric calibration of our images. We also acknowledge the support of the RTN Euro3D: 'Promoting 3D spectroscopy in Europe'. Thanks to the anonymous referee for valuable comments and suggestions that have contributed to improve this paper.

REFERENCES

Allard E. L., Peletier R. F., Knapen J. H., 2005a, ApJ, 633, L25
Allard E. L., Peletier R. F., Knapen J. H., 2005b, in de Grijs R., González Delgado R. M., eds, Astrophysics & Space Science Library, Vol., 329, Starbursts: From 30 Doradus to Lyman Break Galaxies. Springer-Verlag, Dordrecht
Arribas S., Mediavilla E., 1993, ApJ, 410, 552
Arribas S., Mediavilla E., 1994, ApJ, 437, 149
Arribas S., Mediavilla E., Rasilla J. L., 1991, ApJ, 369, 260
Arribas S. et al., 1999, SPIE, 3355, 821
Battaner E., Mediavilla E., Guijarro A., Arribas S., Florido E., 2003, A&A, 401, 67
Begeman K. G., 1989, A&A, 223, 47
Bingham R. G., Gellatly D. W., Jenkins C. R., Worswick S. P., 1994, SPIE, 2198, 56
Canzian B., 1993, ApJ, 414, 487
Canzian B., Allen R. J., 1997, ApJ, 479, 723
Delgado R. M. G., Cerviño M., Martins L. P., Leitherer C., Hauschildt P. H., 2005, MNRAS, 357, 945
Ferrarese L. et al., 1996, ApJ, 464, 568
García-Burillo S., Sempere M. J., Combes F., Neri R., 1998, A&A, 333, 864
García-Lorenzo B., Arribas S., Mediavilla E., 2001, A&A, 378, 787
Heckman T. M., Lehnert M. D., Strickland D. K., Armus L., 2000, ApJS, 129, 493
Hernandez O., Wozniak H., Carignan C., Amram P., Chemin L., Daigle O., 2005, ApJ, 632, 253
Knapen J. H., Beckman J. E., Shlosman I., Peletier R. F., Heller C. H., de Jong R. S., 1995a, ApJ, 443, L73
Knapen J. H., Beckman J. E., Heller C. H., Shlosman I., de Jong R. S., 1995b, ApJ, 454, 623
Knapen J. H., Shlosman I., Heller C. H., Rand R. J., Beckman J. E., Rozas M., 2000, ApJ, 528, 219
Knapen J. H., Pérez-Ramírez D., Laine S., 2002, MNRAS, 337, 808
Knapen J. H., de Jong R. S., Stedman S., Bramich D. M., 2003, MNRAS, 344, 527 (erratum MNRAS, 346, 333)
Mediavilla E., Arribas S., Rasilla J. L., 1992, ApJ, 396, 517
Mediavilla E., Guijarro A., Castillo-Morales A., Jiménez-Vicente J., Florido E., Arribas S., García-Lorenzo B., Battaner E., 2005, A&A, 433, 79
Merrifield M. R., Kuijken K., 1995, MNRAS, 274, 933
Merrifield M. R., Rand R. J., Meidt S. E., 2006, MNRAS, 366, L17
Pierce M. J., 1986, AJ, 92, 285
Rand R. J., 1995, AJ, 109, 2444
Rand R. J., Wallin J. F., 2004, ApJ, 614, 142
Roberts L., 1965, Machine Perception of 3-D Solids, Optical and Electro-optical Information Processing. MIT Press, Cambridge, MA
Rupke D. S., Veilleux S., Sanders D. B., 2005, ApJ, 632, 751
Ryder S. D., Knapen J. H., 1999, MNRAS, 302, L7
Sakamoto K., Okumura S., Minezaki T., Kobayashi Y., Wada K., 1995, AJ, 110, 2075
Sarzi M., Rix H. W., Shields J. C., Ho L. C., Barth A. J., Rudnick G., Filippenko A. V., Sargent W. L. W., 2005, ApJ, 628, 169
Schoenmakers R. H. M., Franx M., de Zeeuw P. T., 1997, MNRAS, 292, 349
Sempere M. J., Garcia-Burillo S., 1997, A&A, 325, 769
Sempere M. J., Garcia-Burillo S., Combes F., Knapen J. H., 1995, A&A, 296, 45
Tremaine S., Weinberg M. D., 1984, ApJ, 282, L5 (TW)
Wada K., Sakamoto K., Minezaki T., 1998, ApJ, 494, 236
Wozniak H., Friedli D., Martinet L., Pfenniger D., 1998, A&A, 330, L5
Zurita A., Relaño M., Beckman J. E., Knapen J. H., 2004, A&A, 413, 73

This paper has been typeset from a TEX/LATEX file prepared by the author.